Variability of thermosphere and ionosphere responses to solar flares

Liying Qian,[1] Alan G. Burns,[1] Phillip C. Chamberlin,[2] and Stanley C. Solomon[1]

Received 21 April 2011; revised 24 June 2011; accepted 24 July 2011; published 15 October 2011.

[1] We investigated how the rise rate and decay rate of solar flares affect the thermosphere and ionosphere responses to them. Model simulations and data analysis were conducted for two flares of similar magnitude (X6.2 and X5.4) that had the same location on the solar limb, but the X6.2 flare had longer rise and decay times. Simulated total electron content (TEC) enhancements from the X6.2 and X5.4 flares were ~6 total electron content units (TECU) and ~2 TECU, and the simulated neutral density enhancements were ~15%–20% and ~5%, respectively, in reasonable agreement with observations. Additional model simulations showed that for idealized flares with the same magnitude and location, the thermosphere and ionosphere responses changed significantly as a function of rise and decay rates. The "Neupert Effect," which predicts that a faster flare rise rate leads to a larger EUV enhancement during the impulsive phase, caused a larger maximum ion production enhancement. In addition, model simulations showed that increased $E \times B$ plasma transport due to conductivity increases during the flares caused a significant equatorial anomaly feature in the electron density enhancement in the F region but a relatively weaker equatorial anomaly feature in TEC enhancement, owing to dominant contributions by photochemical production and loss processes. The latitude dependence of the thermosphere response correlated well with the solar zenith angle effect, whereas the latitude dependence of the ionosphere response was more complex, owing to plasma transport and the winter anomaly.

Citation: Qian, L., A. G. Burns, P. C. Chamberlin, and S. C. Solomon (2011), Variability of thermosphere and ionosphere responses to solar flares, *J. Geophys. Res.*, *116*, A10309, doi:10.1029/2011JA016777.

1. Introduction

[2] Solar flares take place throughout the solar atmosphere and produce large (factors of 2–100) and rapid (minutes) increases of solar irradiance in the XUV (X-ray ultraviolet, 1–25 nm) and EUV (extreme ultraviolet, 25–105 nm). This rapid increase of XUV and EUV irradiance instantly enhances ionization in the Earth's upper atmosphere. Ionospheric effects of solar flares, or sudden ionospheric disturbances (SID), have been studied since 1960s owing to their effects on radio communications and navigation systems. The SID phenomena, such as short-wave fadeout, sudden phase anomaly, sudden frequency deviation, and sudden increase of total electron content (TEC), were well investigated using Doppler sounding systems in the 1960s and 1970s. These results were reviewed by *Mitra* [1974] and *Davies* [1990]. More recently, real-time high temporal resolution (~1 min) TEC measurements by the ground-based Global Positioning System (GPS) network have advanced our understanding of the ionospheric response to solar flares. These data have been collected to form global TEC maps [e.g., *Rideout and Coster*, 2006; *Coster and Komjathy*, 2008]. Observations of terrestrial effects of solar flares have recently been extended to the neutral atmosphere. Neutral density response near 400 km has been obtained from accelerometer measurements of non-gravitational accelerations on the Challenging Minisatellite Payload (CHAMP) and the Gravity Recovery and Climate Experiment (GRACE) satellites [*Lühr et al.*, 2004; *Sutton et al.*, 2006].

[3] GPS observations indicated that the mean amplitude of TEC responses to flares depended on flare location on the Sun [*Afraimovich et al.*, 2002; *Tsurutani et al.*, 2005; *Liu et al.*, 2006]. *Tsurutani et al.* [2005] compared GPS measurements of the 28 October 2003 (X17) and 4 November 2003 (X28) solar flares; the X17 flare located near the center of the solar disk, whereas the X28 flare was at the limb; as a result, the TEC increase during the X17 flare was ~5 times the TEC increase during the X28 flare. We would note that the NOAA/SWPC reports the 4 November 2003 flare as X17.4, but X28 is the appropriate classification for the flare that has been used by researchers [e.g., *Tsurutani et al.*, 2005]. It is an extrapolation/estimation as the GOES XRS detectors saturate at X17.2 levels. *Qian et al.* [2010] investigated how the location of a flare on the solar disk affects the thermosphere and ionosphere

[1]High Altitude Observatory, National Center for Atmospheric Research, Boulder, Colorado, USA.
[2]Solar Physics Laboratory, NASA Goddard Space Flight Center, Greenbelt, Maryland, USA.

Copyright 2011 by the American Geophysical Union.
0148-0227/11/2011JA016777

response to it. They found that most emission lines in the XUV are optically thin, and thus flare enhancement of the XUV only weakly depends on the location of a flare; but in the EUV many important lines and continua are optically thick, so flare enhancement of EUV is significantly weaker for flares located near the solar limb compared with flares near the solar disk center, owing to absorption by the solar atmosphere. These different effects of flare location on XUV and EUV radiation are important since the XUV and EUV ionize different parts of the thermosphere. The XUV dominates ionization in the lower thermosphere (<~150 km) whereas the EUV dominates ionization in the upper thermosphere. Consequently, flare location has a very small effect on the *E* region and lower thermosphere but has a large effect on the *F* region ionosphere and upper thermosphere. Therefore, it can have a potentially significant impact on operations such as radio communication, GPS, and satellite drag. *Zhang et al.* [2011] conducted statistical analysis and found that at the same X-ray class, flares near the solar disc center have much larger effects on the ionospheric TEC than those near the solar limb region.

[4] A question arises as to whether thermosphere and ionosphere responses scale proportionally to the intensity of flares that have the same location on the Sun. Flare intensity is classified by its soft X-ray brightness as observed by Geostationary Operational Environmental Satellites (GOES) X-Ray Sensor (XRS) [*Garcia*, 2000]. Without the location factor, the soft X-ray fluxes observed by GOES XRS have been shown to be an accurate representation for the EUV and FUV changes during a solar flare [*Priest*, 1981; *Horan et al.*, 1983]. This is not straightforward, though, as many emissions in the EUV and FUV are formed in different regions of the solar atmosphere containing various parts of the flare structure. *Chamberlin et al.* [2008] conducted a statistical analysis and found that there is a linear relation between irradiance of the XRS 0.1–0.8 nm and irradiance in wavelengths from 0.1 to 14 nm, as they are all coronal emissions, and a power law relation between irradiance of the XRS wavelengths to irradiance of the EUV and FUV wavelengths from 14 to 190 nm, that are formed throughout the solar atmosphere. Since the maximum flux of 0.1–0.8 nm produced by a flare is the most common way for measuring the intensity of solar flares at present, we may expect that without the location factor, the peak amplitudes of neutral density and TEC responses may scale proportionally to the intensity of solar flares as classified by their X-ray brightness, according to the proportional relationship between the soft X-ray enhancement and the EUV enhancement during a solar flare. Nevertheless, the question remains how the duration of solar flares affects this possible relationship.

[5] Furthermore, *Neupert* [1968, 1989] demonstrated that the positive time derivative of the GOES XRS X-ray irradiance (ΔXRS/Δt) is an important factor in quantifying the impulsive phase EUV emissions. This relationship is now referred to as the "Neupert Effect." Impulsive phase studies using the relationship between the $\Delta(XRS)/\Delta t$ and the observations from the Thermosphere Ionosphere Mesosphere Energetics and Dynamics (TIMED) Solar EUV Experiment (SEE) [*Woods et al.*, 2005] once again show a power law relationship between ΔXRS/Δt and EUV irradiance longer than 27 nm [*Chamberlin et al.*, 2008]. These impulsive phase EUV radiations are very strong for those EUV emissions that are formed in the transition region, and are very small in coronal emissions at wavelengths less than 27 nm. This leads to the question of how this Neupert Effect, or the strength of EUV during impulsive phase determined by the risetime of a flare, changes the neutral density and TEC responses.

[6] The purpose of this paper is to examine whether neutral density and TEC responses scale directly to the intensity of solar flares as classified by their X-ray brightness for flares with the same location on the Sun, to investigate how flare risetime and decay time impact thermosphere and ionosphere responses, and to understand the physical mechanisms of these responses. We use the National Center for Atmospheric Research (NCAR) Thermosphere-Ionosphere-Mesosphere-Electrodynamics General Circulation Model (TIME-GCM) [*Roble and Ridley*, 1994] to simulate neutral and electron density responses to idealized flares with the same intensity and location on the solar disk, but with different rise and decay times. Flare spectra estimated by the Flare Irradiance Spectral Model (FISM) [*Chamberlin et al.*, 2007, 2008] are used as solar input to the TIME-GCM for these flare simulations. In addition, TIME-GCM simulations, CHAMP neutral density data, and GPS TEC data are used to examine the thermosphere and ionosphere responses to an X5.4 flare with fast rise (15 min) and short decay (2.5 h) that occurred on 8 September 2005, and an X6.2 flare with slower rise (40 min) and longer decay (5 h) that occurred on 9 September 2005. Both of the flares were located near the solar limb. Diagnostic analysis of the model outputs are carried out to examine the physical and photochemical processes that determine the thermosphere and ionosphere responses to these flares.

2. Model Description

2.1. FISM Solar Flare Model

[7] The Flare Irradiance Spectral Model (FISM) is an empirical model developed for space weather applications. It uses the GOES XRS 0.1–0.8 nm channel, TIMED SEE, Solar Radiation and Climate Experiment (SORCE) Solar Stellar Irradiance Comparison Experiment (SOLSTICE) [*McClintock et al.*, 2000], and *F*10.7 as inputs, to estimate the solar XUV and EUV irradiances at wavelengths from 0.1 to 190 nm at 1 nm resolution with a temporal resolution of 60 s [*Chamberlin et al.*, 2007, 2008]. This is a high enough temporal resolution to model variations due to solar flares, for which few accurate measurements at these wavelengths exist. The flare component of FISM is available from the start of the GOES XRS measurements in 1974 until present. FISM fully quantifies, on all time scales, the changes in the solar irradiance in the wavelength range that directly affects the Earth's thermosphere and ionosphere, and thus can have major affects on satellite drag, radio communications, as well as on the accuracy in the GPS.

2.2. NCAR TIME-GCM

[8] The NCAR TIME-GCM [*Roble and Ridley*, 1994] is a first-principles upper atmospheric general circulation model that solves the fully coupled, nonlinear, hydrodynamic, thermodynamic, and continuity equations of the neutral gas self-consistently with the ion energy, ion momentum, and ion continuity equations. It utilizes a spherical coordinate system fixed with respect to the rotating Earth, with latitude and longitude as the horizontal coordinates and pressure surface as the vertical coordinate. It has a horizontal resolution of 5° × 5°. The pressure interfaces are defined as $lev = \ln(P_0/P)$, and P_0 is a reference pressure at 5×10^{-4} μb. The model has 49 pressure

surfaces covering the altitude range from ~30 km to ~600 km, with *lev* ranging from −17 to 7 and a vertical resolution of one-half scale height. The external forcing of the TIME-GCM are solar irradiance, parameterized using the *F*10.7 index or supplied by measurements or empirical models [*Solomon and Qian*, 2005]; auroral electron precipitation [*Roble and Ridley*, 1987] and ionospheric convection driven by the magnetosphere-ionosphere current system [*Heelis et al.*, 1982]; and the amplitudes and phases of tides from the lower atmosphere [*Hagan and Forbes*, 2002, 2003]. For the investigation in this paper, we will use solar spectra provided by FISM as the solar input for the TIME-GCM.

[9] There is another version of NCAR upper atmospheric models called the thermosphere-ionosphere-electrodynamics general circulation model (TIE-GCM) [*Roble et al.*, 1988; *Richmond et al.*, 1992]. Compared to the TIE-GCM, the TIME-GCM has the advantage of including mesosphere. For solar absorptions, the difference between the TIME-GCM and TIE-GCM is that the TIME-GCM includes absorption in UV wavelengths such as O_2 absorption in Shumann-Runge continuum and Shumann-Runge bands, and O_3 dissociation from the Herbzberg, Hartley, Huggins, and Chapius bands. However, for the XUV and EUV, the TIE-GCM and TIME-GCM use the same solar energy deposition scheme [*Solomon and Qian*, 2005], and photoionization is calculated for the altitude above ~97 km for both the TIME-GCM and the TIE-GCM. Therefore, both models can be used for the solar flare study in this paper. The TIME-GCM will be used to include any possible effect of upward propagating waves, which is not as well represented in the TIE-GCM [*Qian et al.*, 2009].

3. Data

3.1. CHAMP Neutral Density

[10] The CHAMP satellite was launched into a near-circular orbit with an inclination of 87.3° on 15 July 2000 [*Reigber et al.*, 2002]. This high inclination ensures almost complete latitudinal coverage from pole to pole. Neutral density is obtained from accelerometer measurements of nongravitational accelerations on the CHAMP satellite along the orbit [*Sutton et al.*, 2006]. The measured densities are normalized to a constant altitude of 400 km using NRLMSISE00 [*Picone et al.*, 2002]. CHAMP neutral density data has high temporal resolution (~30–60 s) and good spatial resolution (3°), and thus is suitable for flare studies.

3.2. TEC From Ground-Based GPS Network

[11] Ground-based GPS TEC measurements have been available from a global network of GPS stations on a routine basis since at least 2001 [*Rideout and Coster*, 2006; *Coster and Komjathy*, 2008]. The MIT Automated Processing of GPS (MAPGPS) software suite [*Rideout and Coster*, 2006] has been developed to calculate TEC from the network of worldwide GPS receivers. These TEC estimates are output in 1 degree by 1 degree bins of latitude/longitude every 5 min, distributed over those locations where data are available and are stored in Haystack's Madrigal database. Recently, the MAPGPS processing code was significantly enhanced to improve error handling. Errors are now tracked throughout the processing, and random and correlated errors are handled separately. This allows optimal estimation of binned measurements and allows error values to be calculated independently for each binned measurement. The bin-to-bin variability in the TEC measurements was greatly reduced using this approach.

4. Results

4.1. Simulated Response to Idealized Flares

[12] In order to investigate whether thermosphere and ionosphere responses scale proportionally to the intensity of flares with the same location on the Sun, and how flare risetime and decay time impact thermosphere and ionosphere responses, we constructed three idealized flares: a control flare, a faster rise flare, and a longer decay flare. These three flares are simulated GOES XRS 0.1–0.8 nm light curves with a single, isolated variable (e.g., risetime) that was then used as input to drive the FISM model while holding all other model variables constant (e.g., flare location, X-ray peak intensity, and decay time). The control flare was a simulated lognormal GOES XRS light curve fit to the X10 flare on 20 January 2004, located near the center of the solar disk. It started at 12:00 UT, reached peak at 12:40 UT, and returned to its preflare irradiance at 16:00 UT. The faster rise flare is the same as the control flare except that its risetime was reduced to half, and the longer decay flare is the same as the control flare except that its decay time was doubled. Figure 1a shows the XUV characteristics of the three flares given by the FISM. In addition, it was assumed that these three flares had a same constant spectral irradiance for their preflare and postflare conditions and the geomagnetic conditions were quiet ($Kp = 1$).

[13] Figure 1b shows the corresponding integrated EUV (27–105 nm) irradiance for the three flares. Unlike the XUV enhancements, the peak EUV enhancements for the three flares are different even though these flares have the same GOES classification. The longer decay flare has the same maximum EUV enhancement as the control flare; however, the faster rise flare has a larger total EUV enhancement during the rise phase. As we mentioned earlier, this is due to the fact that the EUV irradiance is proportional to $\Delta(XRS)/\Delta t$ during the impulsive phase of a flare [*Chamberlin et al.*, 2008], according to the Neupert Effect. There is a kink in the EUV plot shown in Figure 1b. It is due to contributions from the two different phases of the flares, the impulsive phase that provides the initial, quick increase and the gradual phase that provides the second, longer-duration component. The coronal soft X-rays shown in Figure 1a do not have significant impulsive phase contribution and therefore, do not have a kink [*Chamberlin et al.*, 2008].

[14] Since the three flares have the same preflare irradiance and the same soft X-ray peak magnitude and classification, the preflare and flare peak spectra for these flares are the same as shown in Figure 2. The TIME-GCM was run for 20 days using the constant preflare spectral irradiance to reach an equilibrium condition for 20 January 2004, and then run for each of the three cases of the simulated flares occurring on 20 January 2004. The model was also run for this day assuming no solar flare using the constant preflare solar irradiance. All these model simulations assumed geomagnetic quiet conditions to emphasize flare irradiance responses.

[15] Figure 3 shows the neutral temperature and neutral density enhancements at 400 km and 12:00 LT for 20 January 2004, for each case. The enhancements were calculated as

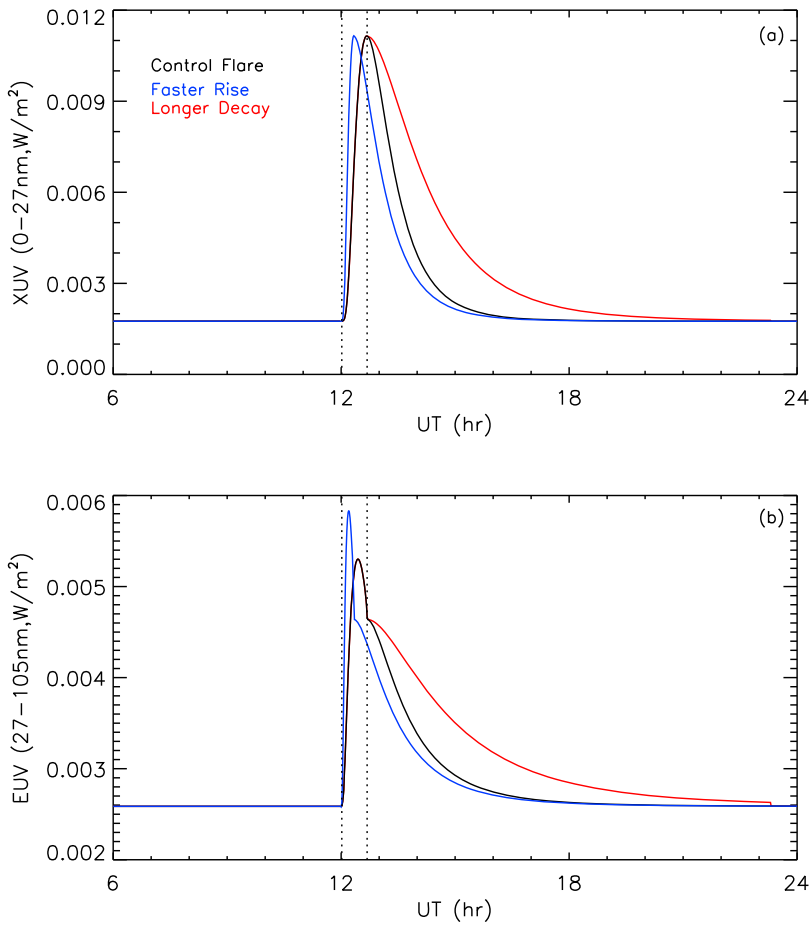

Figure 1. Integrated (a) XUV (0–27 nm) and (b) EUV (27–105 nm), for three assumed X10 near-center solar flares on day 20 of 2004 (a control flare, a faster rise flare, and a longer decay flare). The control flare was assumed to start at 12:00 UT, peak at 12:40 UT (40 min risetime), and recover at 04:00 UT (3 h and 20 min decay time). The faster rise flare had the same characteristics as the control flare except that its rise-time was 20 min. The longer decay flare had the same characteristics as the control flare except that its decay rate was half of the control flare. Black line shows the control flare; blue line shows the faster rise flare; and red line shows the longer decay flare. The dotted lines indicate the universal time of the preflare and the peak of the control flare.

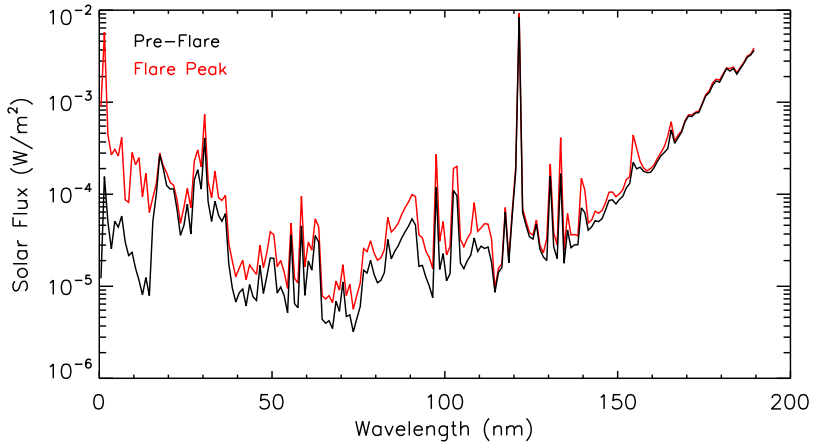

Figure 2. The spectra for the preflare and the peaks of the three X10 flares, provided by FISM. Since the control flare, the faster rise flare, and the longer decay flare have the same intensity (classification), the spectrum at the peak is the same for the three flares.

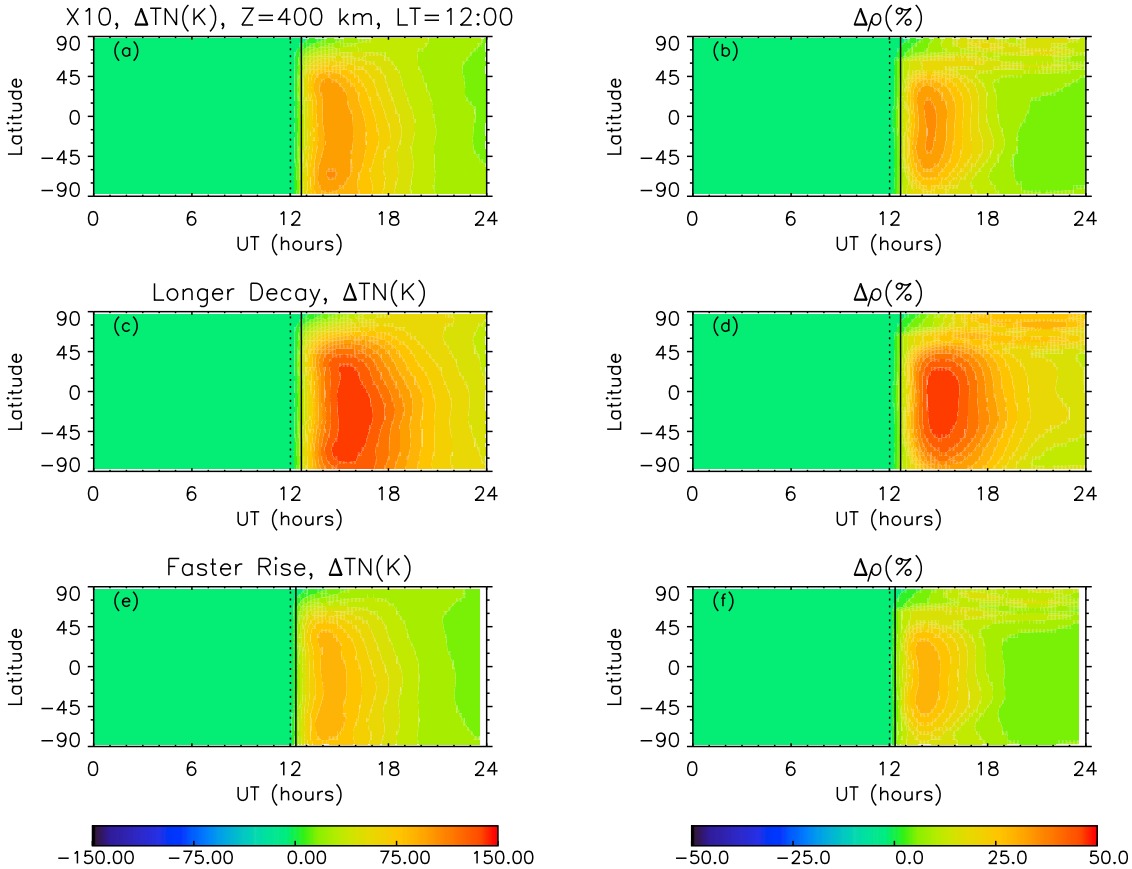

Figure 3. Flare enhancements of neutral temperature (K) and neutral density (%) at 400 km and 12:00 LT: (a) temperature enhancement to the X10 control flare, (b) density enhancement to the X10 control flare, (c) temperature enhancement to the X10 longer decay flare, (d) density enhancement to the X10 longer decay flare, (e) temperature enhancement to the X10 faster rise flare, and (f) density enhancement to the X10 faster rise flare. The flare enhancements are the difference between the simulation results of each flare run and the simulation results assuming no flare. The geomagnetic activity was assumed to be quiet ($Kp = 1$). Dotted line shows the preflare time; solid line shows the flare peaks.

the difference between the flare and nonflare runs. The altitude 400 km was chosen since this is in the altitude range where low-Earth satellites fly. The thermosphere response to the longer decay flare was much stronger than to the control flare whereas the response to the faster rise flare was slightly weaker than to the control flare. The maximum temperature enhancements near subsolar latitudes (~22.5°S) (and the time to reach these maximum enhancements after the flares reached peaks) were ~145 K (185 min), ~105 K (130 min), and 90 K (140 min) for the longer decay flare, the control flare, and the faster rise flare, respectively; whereas the maximum neutral density responses near the subsolar latitude (and the time to reach these maximum enhancements after the flares reached peaks) were ~50% (140 min), ~37% (115 min), and ~31% (125 min) for the longer decay flare, the control flare, and the faster rise flare, respectively. Sudden increases of XUV and EUV during solar flares enhance ionization [*Qian et al.*, 2010], which heats the thermosphere. The heating due to enhanced ionization causes these maximum enhancements of neutral density. The heating will then change circulation, which in turn change composition and cause further neutral density changes. However, these latter changes occur about a couple hours after the initial density enhancement, and are much weaker [*Qian et al.*, 2010]. Figure 3 also shows that there are bands of enhanced neutral density in the northern high-latitude region. These density enhancements are likely caused by changes of circulation patterns due to flares. Wind resulting from heating will impact day-night circulation, large-scale summer to winter circulation, and high-latitude auroral circulation, causing additional convergence in the winter high-latitude region, as well as a shift of convergence zone in the area. This convergence changes temperature and composition, which in turn changes neutral density.

[16] Figure 4 shows the N_mF_2 and h_mF_2 enhancements at 12:00 LT on 20 January 2004 for each flare, with UT as the x axis and latitude as the y axis. The geomagnetic equator is also shown in Figure 4. Similarly to Figure 3, the flare enhancement in Figure 4 was calculated by subtracting the nonflare run results from the flare-run results for each case. Even though the time evolution and morphology of the flare responses in the ionosphere shown in Figure 4 are very different from those in the thermosphere shown in Figure 4,

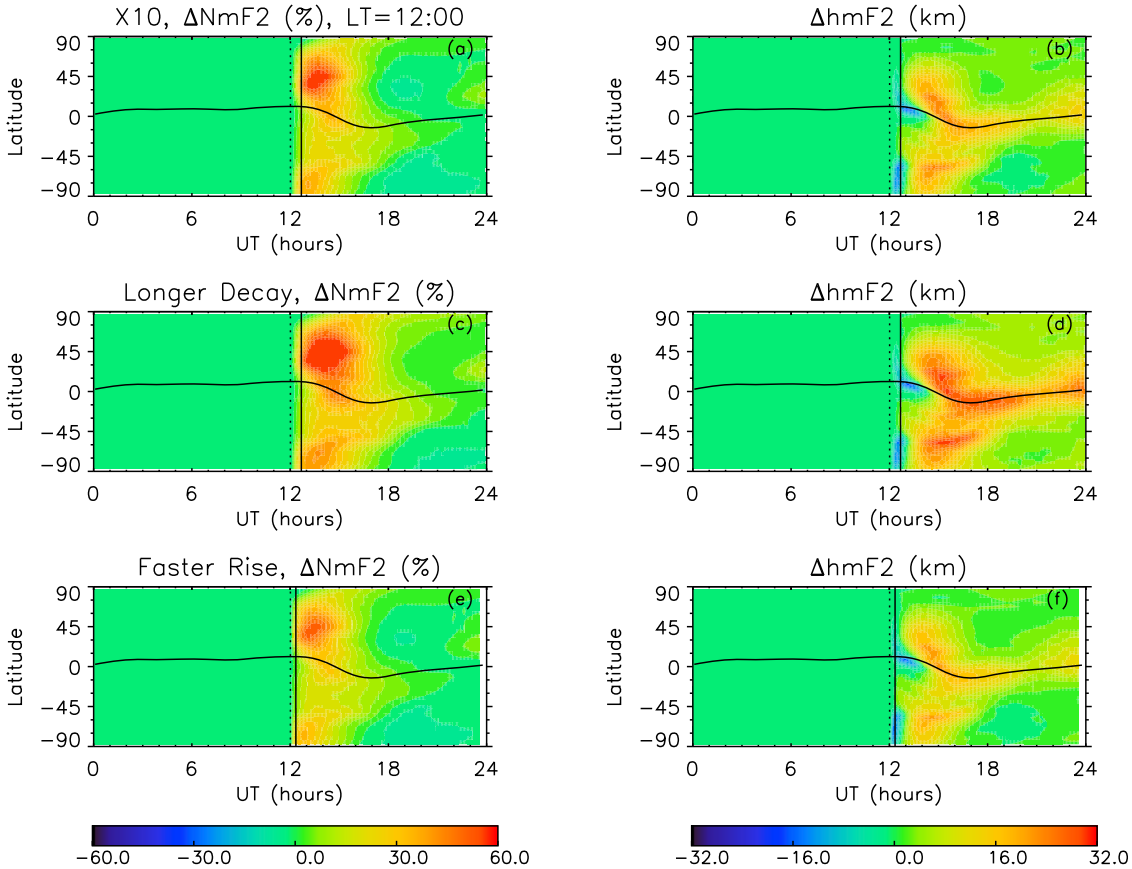

Figure 4. Flare enhancements of N_mF_2 (%) and h_mF_2 (km) at 12:00 LT to the three assumed flares: (a) N_mF_2 enhancement to the X10 control flare, (b) h_mF_2 enhancement to the X10 control flare, (c) N_mF_2 enhancement to the X10 longer decay flare, (d) h_mF_2 enhancement to the X10 longer decay flare, (e) N_mF_2 enhancement to the X10 faster rise flare, and (f) h_mF_2 enhancement to the X10 faster rise flare. The flare enhancements are the difference between the simulation results of each flare run and the simulation results assuming no flare. The geomagnetic activity was assumed to be quiet (Kp = 1). Dotted line shows the preflare time; vertical solid line shows the flare peaks; and horizontal solid line shows the geomagnetic equator.

it is evident that, similar to the thermosphere responses, the longer decay flare caused much stronger enhancements of N_mF_2 and h_mF_2 compared to the control flare, whereas the faster rise flare caused slightly weaker responses compared to the control flare.

[17] Figures 3 and 4 showed that for the three flares with the same magnitude and the same location, the thermosphere and ionosphere responses changed significantly as the rise and decay rates changed. Increasing the decay time of the control flare had a large effect on enhancing the thermosphere and ionosphere responses, whereas reducing the risetime of the control flare had a relatively small effect on weakening the responses. This is due to the fact that flare risetime is usually short (<1 h) compared to decay time (of the order of several hours), thus more flare energy is usually contained in the decay phase. This can be illustrated by examining the total energy increases during the flares. The total energy increases for the longer decay flare, the control flare, and the faster rise flare were 2.29 W/m^2, 1.35 W/m^2, and 1.17 W/m^2, respectively. The difference in the total energy increases between the longer decay flare and the control flare is significantly larger than that between the faster rise flare and the control flare. Consequently, the difference in the decay time played a larger role in determining flare responses compared to the difference in the risetime. In these simulations, we examined how one flare characteristic affected the flare responses when all the other characteristics were fixed, thus the total energy was not fixed. Future studies will investigate how the intensity, risetime, and decay time of a flare impact thermosphere and ionosphere responses when the total radiated energy from a flare is a constant.

[18] We mentioned earlier the Neupert Effect, which leads to a larger EUV enhancement during the fast rising flare as shown in Figure 1b. Here we examine the impact of this relationship. Figure 5 compares the ion production enhancements for the three flares. Overplotted on Figure 5 is the integrated EUV (27–105 nm) irradiance. The larger EUV enhancement of the faster rise flare caused a larger maximum enhancement of ion production compared to the control flare and the longer decay flare. However, this larger enhancement of ion production did not cause significantly larger enhancements of electron density, neutral temperature, and neutral

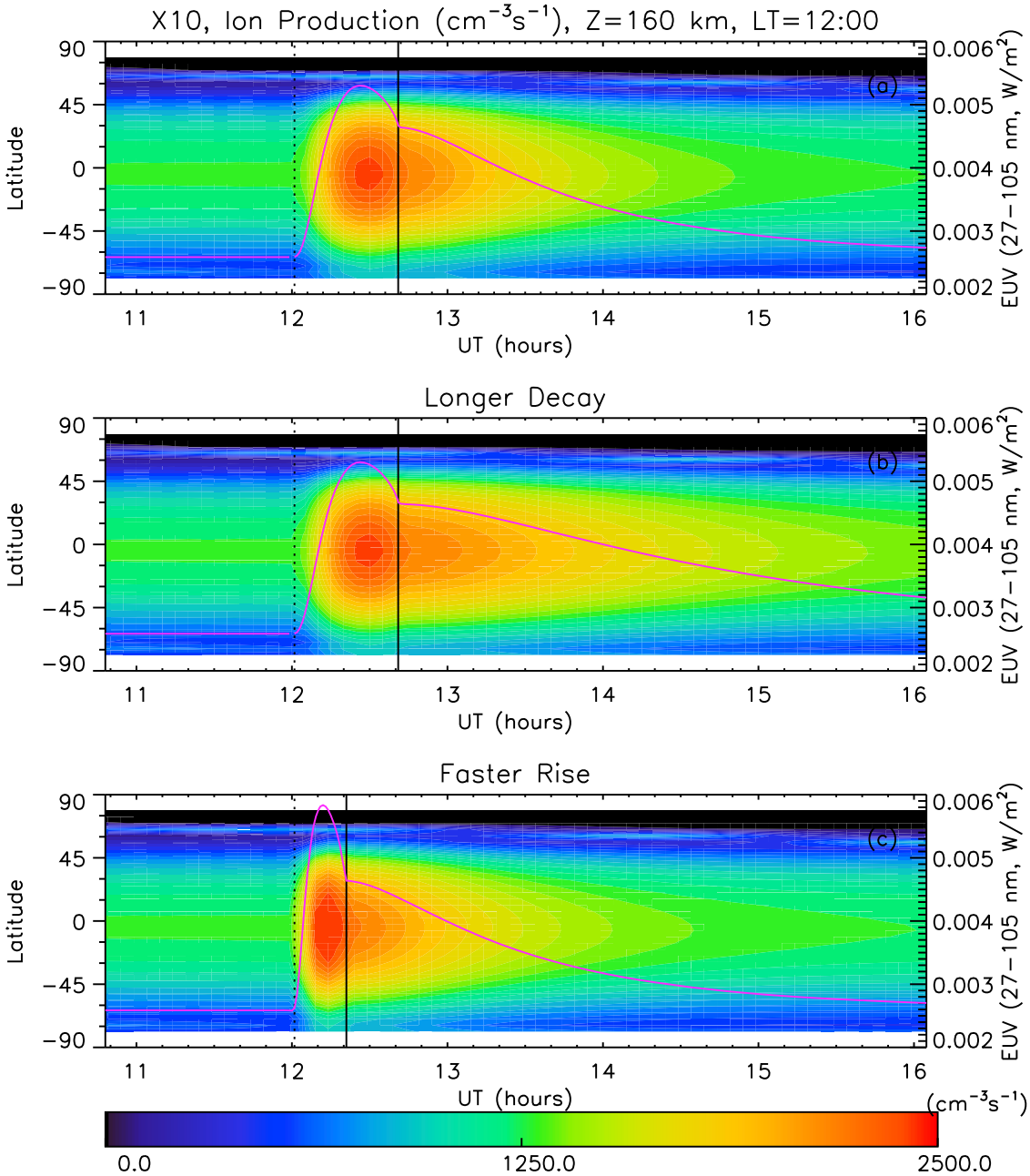

Figure 5. Ion production rate at 160 km and 12:00 LT responding to the three assumed flares: (a) simulated ion production rate for the X10 control flare, (b) simulated ion production rate for the X10 longer decay flare, and (c) simulated ion production rate for the X10 faster rise flare. Black dotted line shows the preflare time; black solid line shows the flare peaks; and magenta solid line shows the integrated EUV (27–105 nm) for the flares.

density. Figures 3 and 4 showed that the thermosphere and ionosphere responses of the faster rise flare were slightly weaker than the control flare. Therefore, the Neupert Effect of the faster rise flare increased the maximum enhancement of the ion production owing to the larger EUV enhancement during the rising phase of the faster rise flare, but the maximum enhancements of the neutral temperature and density, as well as electron density, were slightly weaker than the control flare owing to the reduction of the risetime, and thus the total energy.

4.2. Latitude Dependence of the Flare Responses

[19] The ionosphere response (Figure 4) shows a much more complicated latitudinal variation compared with the thermosphere response (Figure 3). We calculated maximum enhancements in the thermosphere and ionosphere to quantify the latitude dependences. Figure 6 shows the maximum enhancements of neutral temperature and neutral density responding to the X10 control flare, at 400 km and 12:00 LT, as well as the maximum enhancements of N_mF_2 and TEC at 12:00 LT. The

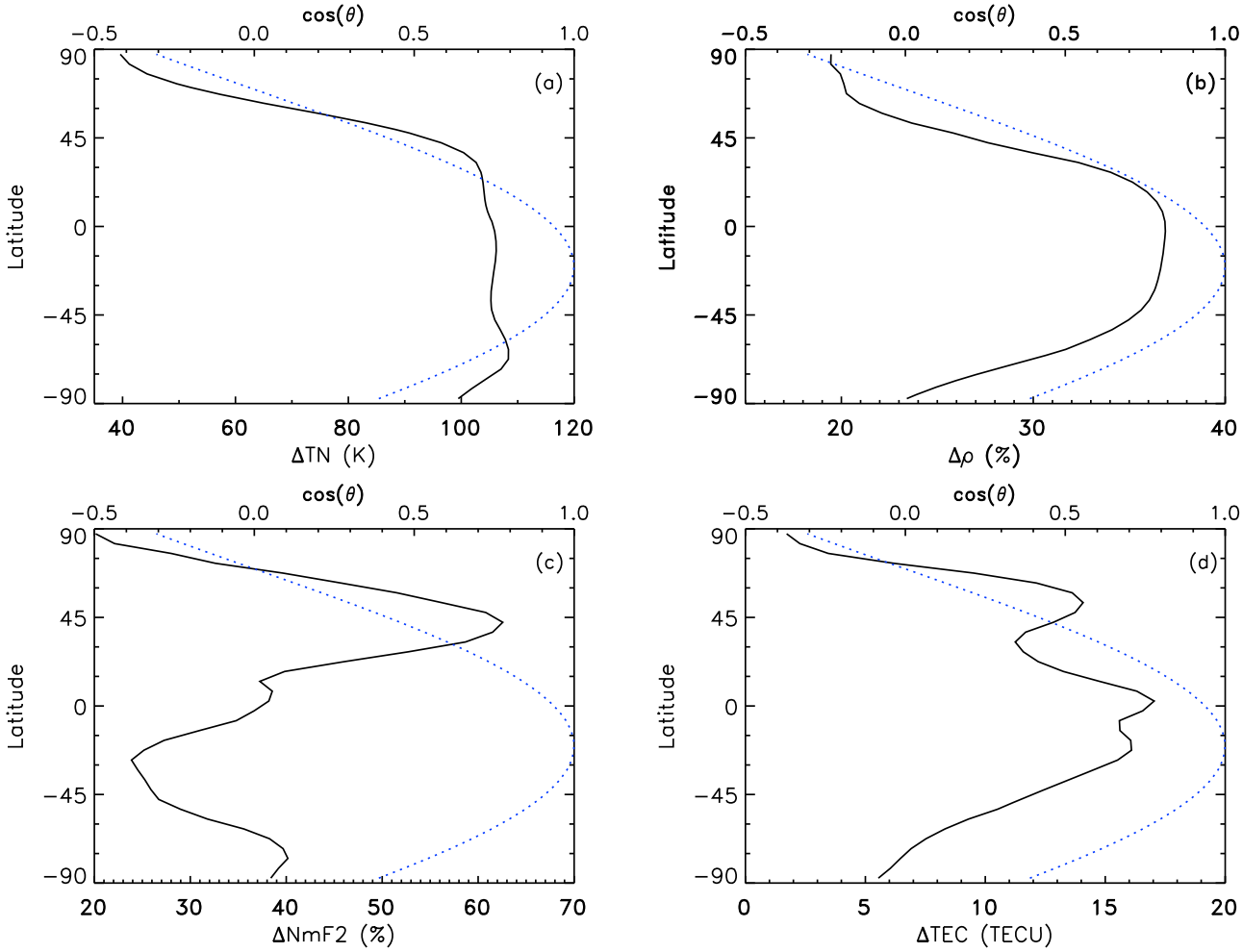

Figure 6. Latitude dependence of the flare responses in the thermosphere and ionosphere, responding to the X10 control flare on 20 January 2004: (a) maximum enhancement of neutral temperature (K) at 400 km and 12:00 LT, (b) maximum enhancement of neutral density (%) at 400 km and 12:00 LT, (c) maximum enhancement of N_mF_2 (%) at 12:00 LT, and (d) maximum enhancement of TEC (TECU) at 12:00 LT. Solid line shows maximum enhancements of the variables; dotted line shows cosine of the solar zenith angle. One TECU is 10^{12} el cm^{-2}.

dotted lines in the plots are the cosine of the solar zenith angle on 20 January 2004. Since the time it takes for each variable to reach its maximum enhancement is different at each latitude, the maximum responses shown in Figure 6 is not at one particular fixed time. The flare enhancements of neutral temperature and neutral density are largely determined by the solar zenith angle effect (Figures 6a and 6b). On the other hand, the latitude dependence of N_mF_2 (Figure 6c) does not follow the solar zenith angle effect. Diagnostic analysis of the model results indicated that this is due to the flare responses of plasma transport by $E \times B$ drifts, neutral wind, and ambipolar diffusion. In addition, the N_mF_2 enhancement shows a peak at midlatitudes in the winter hemisphere due to the winter anomaly [e.g., *Keating and Prior*, 1968; *Hedin et al.*, 1974; *Jacchia*, 1974]. The effects of $E \times B$ drift and winter anomaly effects are also evident in the TEC enhancement (Figure 6d). The TEC enhancement, however, mainly follows the solar zenith angle effect. This is due to the dominant contributions from photochemical production and loss processes, discussed in section 4.3.

4.3. Simulated and Observed Flare Responses

[20] An X5.4 flare occurred on 8 September 2005 and an X6.2 flare occurred on 9 September 2005, as measured by GOES 10 and shown in Figure 7a. The X5.4 flare started at 20:50 UT, peaked at 21:05 UT, and returned to its preflare irradiance at 23:40 UT. The X6.2 flare started at 19:20 UT, peaked at 20:00 UT, and returned to its preflare irradiance at 01:00 UT on 10 September 2005. The risetimes for the X5.4 and X6.2 flares were 15 min and 40 min, respectively, and the decay times for the X5.4 and X6.2 flares were 2 h 35 min and 5 h. Both the flares were located near the limb of the solar disk. The two flares had similar soft X-ray peak intensities (within 15%), but the X5.4 flare had a faster risetime and shorter decay time compared with the X6.2 flare. Figure 7b shows CHAMP neutral density along the dayside orbits from 8 September 2005 to 10 September 2005. The local time is 10:30 LT. Figure 7c is the TIME-GCM simulated neutral density sampled along the CHAMP dayside orbits. FISM

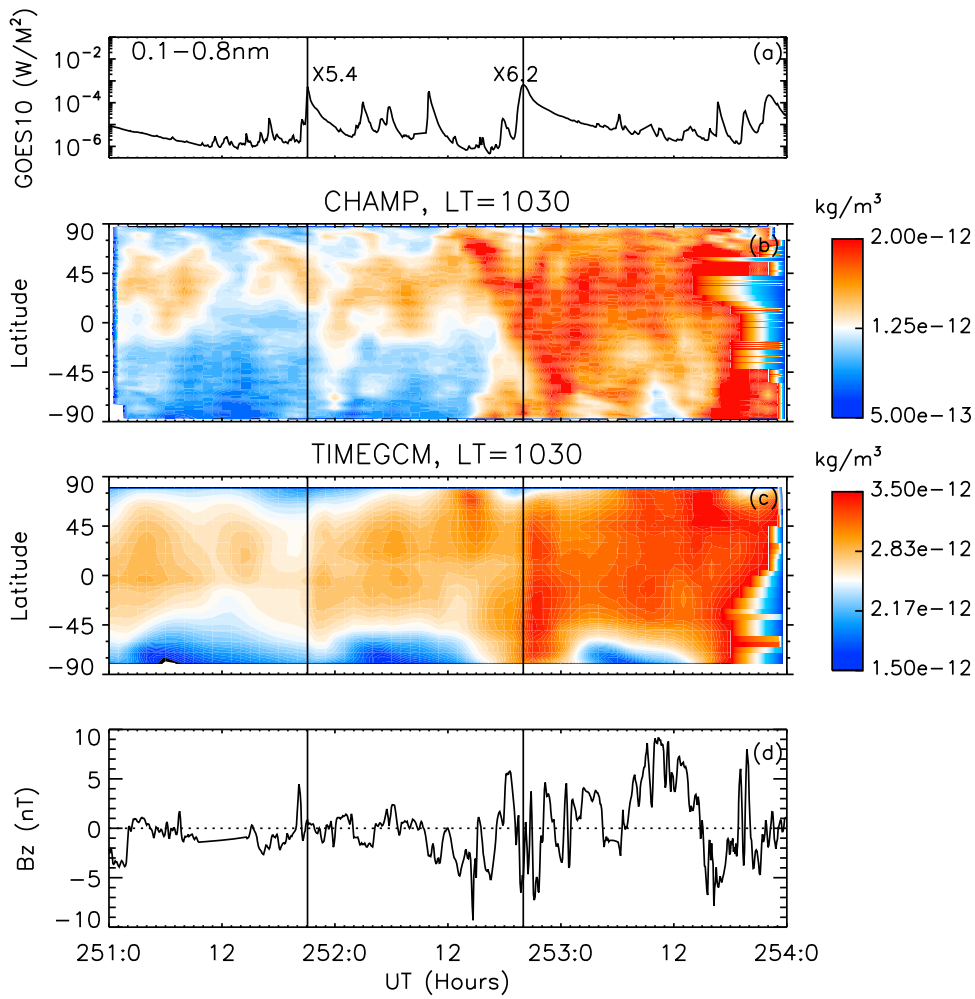

Figure 7. (a) GOES 10 0.1–0.8 nm soft X-Ray for 8–10 September 2005. An X5.4 flare occurred on 8 September 2005, and an X6.2 flare occurred on 9 September 2005. The X5.4 flare started at 20:50 UT, peaked at 21:05 UT, and returned to its preflare irradiance at 23:40 UT. The X6.2 flare started at 19:20 UT, peaked at 20:00 UT, and returned to its preflare irradiance at 01:00 UT on 10 September 2005. Both the flares are located near the limb of the solar disk. The solid vertical lines are the flare peaks. (b) Neutral density observed by CHAMP along CHAMP's dayside orbits at local time 10:30. (c) TIME-GCM simulated neutral density sampled along the CHAMP orbits. (d) Interplanetary magnetic field Bz for these three days.

flare spectra driven by the actual GOES XRS data were used for these simulations. The TIME-GCM simulations show a weak neutral density enhancement to the X5.4 flare (~5%), but a much stronger response to the X6.2 flare (~15–20%) near subsolar latitudes. The CHAMP neutral density does not show a clear response to the X5.4 flare but shows a rather strong density enhancement during the X6.2 flare. However, there was geomagnetic activity ($Kp = 4$) before and during the X6.2 flares as shown in the interplanetary magnetic field Bz plot (Figure 7d) that appears to have contributed to the neutral density enhancement. Figure 7b shows evidence of traveling disturbance in neutral density enhancement [*Bruinsma and Forbes*, 2007], probably due to geomagnetic activity. As a result, it is hard to discern flare response from geomagnetic effect for this flare. This was the reason that we conducted the investigation described in sections 4.1 and 4.2 using the idealized flares.

[21] There is discrepancy between the absolute magnitudes of TIME-GCM density and CHAMP density (Figure 7). As we know that neutral density decreases exponentially with altitude. The TIME-GCM is a pressure model. The difficulty of assigning altitudes to pressure surfaces introduces this discrepancy. However, electron density is calculated self-consistently with respect to composition on pressure surfaces in the TIME-GCM. The geometric altitude assignment does not affect this relationship and TIME-GCM total electron content is consistent with observations [*Qian et al.*, 2010].

[22] Figure 8 shows the TEC for the preflare (19:20 UT), at the flare peak (20:00 UT), and the TEC enhancement for the X6.2 flare, observed by the ground-based GPS network and simulated by the TIME-GCM. FISM flare spectra were used for these simulations. The TEC difference between 20:00 UT and 19:20 UT from the previous day (8 September 2005) was subtracted from the corresponding TEC difference on

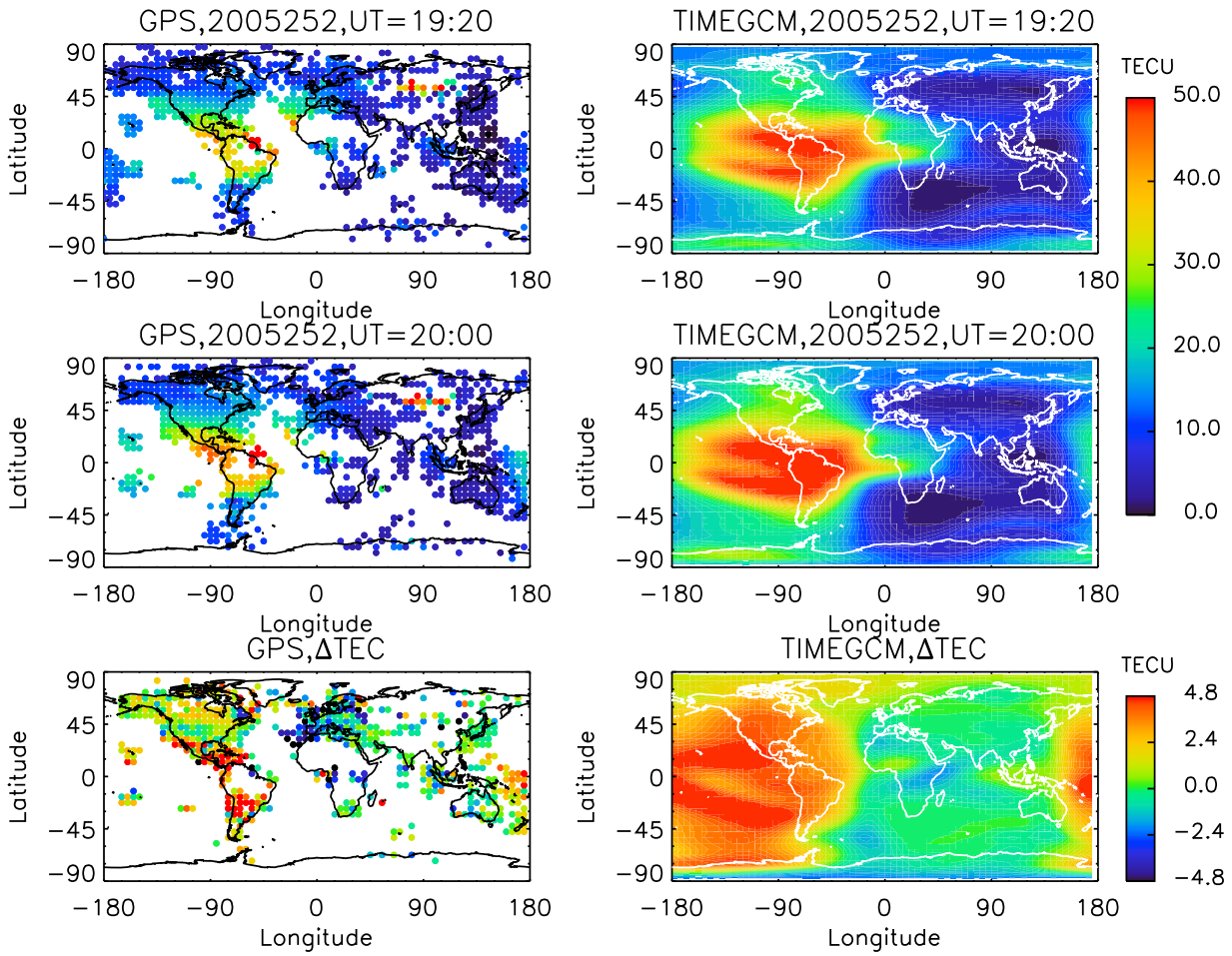

Figure 8. Comparisons of TEC observed by the ground-based GPS network and TEC simulated by the TIME-GCM responding to the X6.2 near-limb flare that occurred on 9 September 2005. (left) GPS measurements of TEC for preflare, flare peak, and TEC enhancement. (right) TIME-GCM simulations of TEC for preflare, flare peak, and TEC enhancement. Preflare is ~19:20 UT; flare peak is ~20:00 UT. ΔTEC equals TEC difference between 20:00 and 19:20 UT on 9 September 2005 minus TEC difference between 20:00 and 19:20 UT on 8 September 2005. FISM solar spectra were used as solar input for the TIME-GCM. One TECU is 10^{12} el cm^{-2}.

9 September 2005, to obtain the flare-induced TEC enhancement shown in Figure 8. GPS observations were incomplete in terms of global coverage, but the TEC difference between the preflare and the flare peak is evident. The maximum TEC enhancement was ~5–6 total electron content units (TECU, 1 TECU = 10^{12} el cm^{-2}). The TIME-GCM simulated TEC is consistent with the GPS observations, especially in the morphology and magnitude of the TEC enhancement.

[23] Figure 9 shows TEC for the preflare (20:50 UT), flare peak (21:05 UT), and the TEC enhancement for the X5.4 flare, observed by the ground-based GPS network and simulated by the TIME-GCM. Similarly, the TEC difference between 21:05 UT and 20:50 UT on the previous day (7 September 2005) was subtracted from the corresponding TEC difference on 8 September 2005 to obtain the flare-induced TEC enhancement shown in Figure 9. The model simulated TEC enhancement is ~2 TECU for this flare. The TEC enhancement observed by the GPS network is also small, consistent with the simulated TEC enhancement.

[24] In Figure 8, the TEC enhancement shows a distinct equatorial anomaly feature. The question arises as to why this occurs, and thus whether this is part of the flare response due to locally produced $E \times B$ drift or whether it is caused by geomagnetic activity. Therefore, we ran the model assuming a constant Kp index ($Kp = 1$) but included the solar irradiance variation. Flare enhancements of variables were then calculated as the difference between 20:00 UT and 19:20 UT on 9 September 2005 minus the difference between 20:00 UT and 19:20 UT on 8 September 2005. Figure 10a shows the enhancement of $E \times B$ at the model pressure level +1.75, which is located just below the F_2 peak. The flare response of $E \times B$ caused the equatorial anomaly morphology of the flare enhancement of electron density at this level (Figure 10b). The TEC enhancement shows a weak equatorial anomaly feature (Figure 10c). This is due to the fact that the TEC enhancement is the integration of the flare enhancements in the E, F_1, and F_2 regions. Since the E and F_1 regions are dominated by the photochemical production and

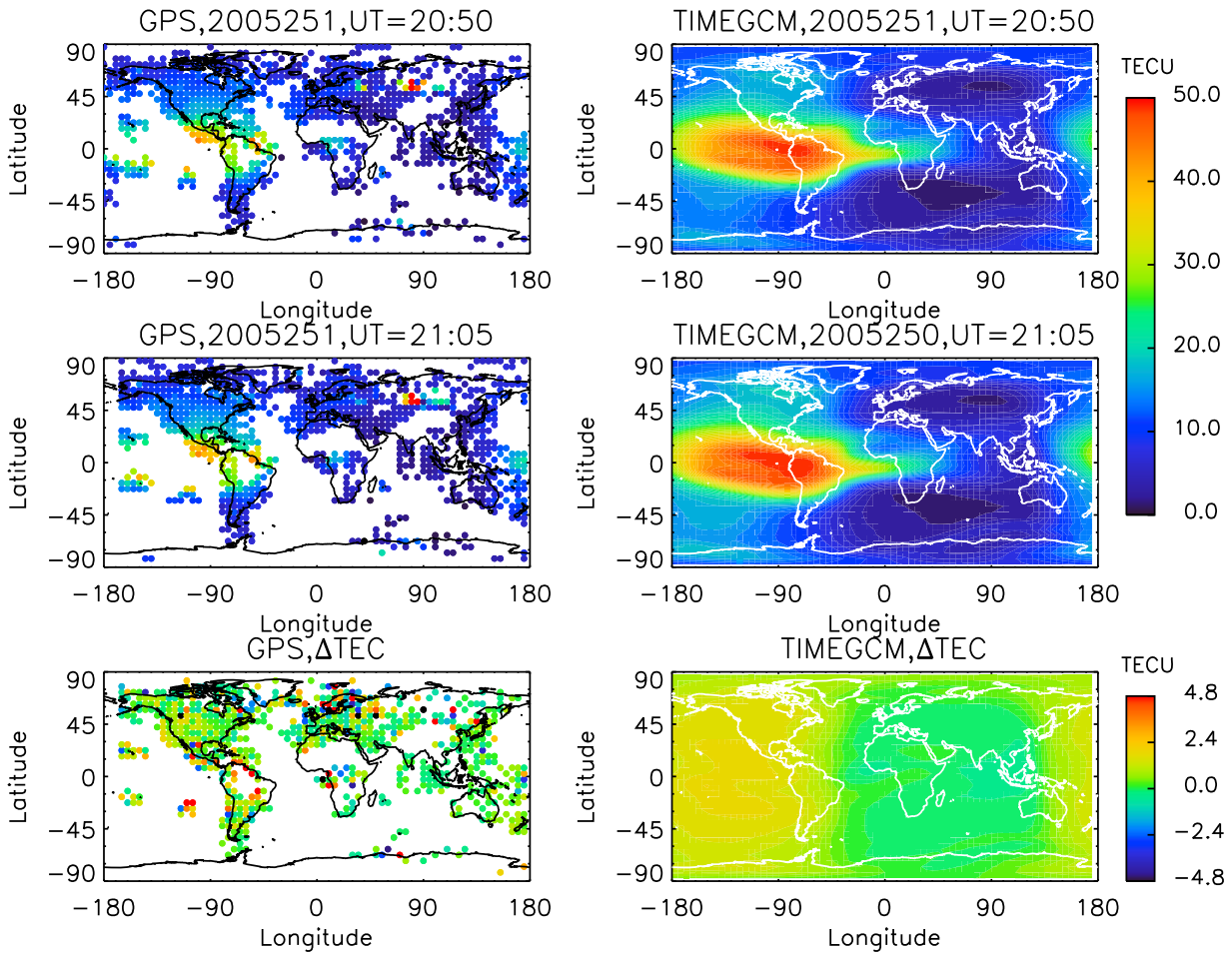

Figure 9. Comparisons of TEC observed by the ground-based GPS network and TEC simulated by the TIME-GCM responding to the X5.4 near-limb flare that occurred on 8 September 2005. (left) GPS measurements of TEC for preflare, flare peak, and TEC enhancement. (right) TIME-GCM simulations of TEC for preflare, flare peak, and TEC enhancement. Preflare is ~20:50 UT; flare peak is ~21:05 UT. ΔTEC equals TEC difference between 21:05 and 20:50 UT on 8 September 2005 minus TEC difference between 21:05 and 20:50 UT on 7 September 2005. FISM solar spectra were used as solar input for the TIME-GCM. One TECU is 10^{12} el cm^{-2}.

loss processes, and photochemical processes still dominate at the +1.75 pressure level, the equatorial anomaly feature in the TEC enhancement was weak owing to the dominant contributions by the photochemical production and loss processes, even though the flare response of plasma transport caused a distinct equatorial anomaly feature in the electron density enhancement in the F_2 layer. There was geomagnetic activity prior and during the X6.2 flare as shown in Figure 7d. The equatorial anomaly feature shown in the TEC enhancement in Figure 8 could be effects of the disturbance dynamo or the effects of penetration electric fields due to geomagnetic activity. In estimating flare responses of TEC enhancement using global GPS data, the TEC difference between the universal time at the flare peak and the preflare of the previous day is usually calculated and subtracted from the TEC difference between the universal time at the flare peak and the preflare on a flare day [*Tsurutani et al.*, 2005; *Woods et al.*, 2008; *Qian et al.*, 2010]. This is also the method that we used for the TEC enhancements shown in Figures 8 and 9. The purpose of this calculation is to remove the local time effects. However, if the difference in geomagnetic forcing between the two days is large, geomagnetic effects will be introduced to the calculation. The *Kp* index of 9 September for 18:00 UT to 21:00 UT was 4.3 whereas it was 1.7 for the previous day, and this significant difference in geomagnetic forcing caused the strong equatorial anomaly feature in the TEC enhancements shown in Figure 8. Therefore, care must be taken in interpreting flare enhancement of TEC using GPS data.

[25] TEC changes in some regions were negative at the night side (Figure 10c). This is interesting since neither such a quick response nor negative values were expected on the night side. A similar pattern of negative changes is shown in the electron density variation in the F_2 layer (Figure 10b), indicating that this is likely an F_2 layer phenomenon. These negative changes may be caused by negative changes of $E \times B$

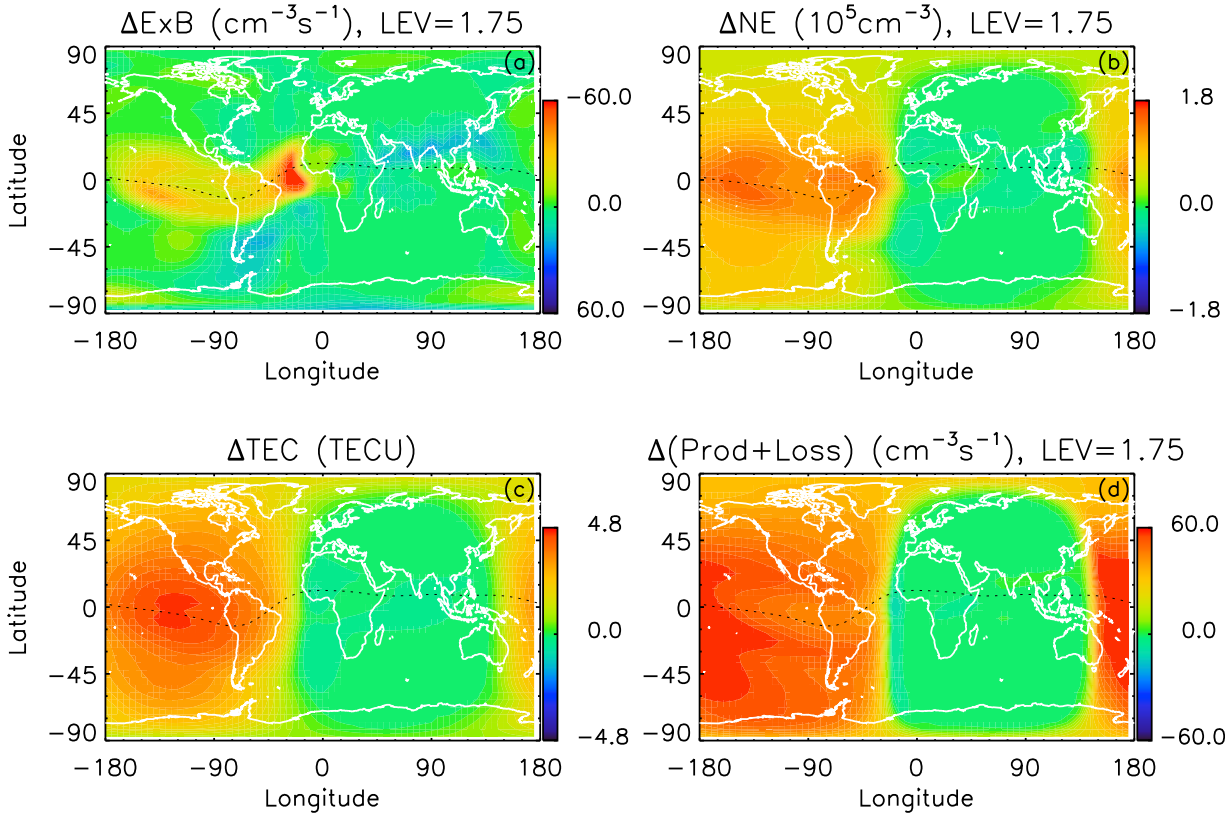

Figure 10. (a) TIME-GCM simulated enhancement of $E \times B$ during the X6.2 flare at *lev* = 1.75. $\Delta E \times B$ equals $E \times B$ difference between 20:00 and 19:20 UT on 9 September 2005 minus $E \times B$ difference between 20:00 and 19:20 UT on 8 September 2005. The simulation assumed constant geomagnetic forcing (*Kp* = 1) for 8–9 September 2005. FISM solar spectra were used as solar input for the TIME-GCM. (b) The corresponding electron density enhancement at *lev* = 1.75. (c) The corresponding TEC enhancement. One TECU is 10^{12} el cm^{-2}. (d) The corresponding enhancement of the sum of the ion production and loss at *lev* = 1.75.

(Figure 10a) and increased photochemical loss (Figure 10d). Further study is needed to understand this phenomenon.

5. Summary and Conclusions

[26] In this paper, we investigated how the thermosphere and ionosphere respond to flares with the same magnitude and same location, and how flare risetime and decay time affect these thermosphere and ionosphere responses. The TIME-GCM was used to simulate the thermosphere and ionosphere responses to an idealized X10 center flare with 40 min risetime and 3 h 20 min decay time, a flare that was otherwise the same as the control flare except that its risetime was reduced to half, and a flare that was otherwise the same as the control flare except that its decay time was doubled. All three flares were assumed to start at 12:00 UT on day 20 of 2004, with a same constant irradiance for the preflare and postflare times, under geomagnetic quiet conditions (*Kp* = 1). Model simulations show that for the three flares with the same magnitude and the same location, the thermosphere and ionosphere responses changed significantly as the rise and decay rates changed. Increasing the decay time of the control flare had a large effect in enhancing the thermosphere and ionosphere responses, whereas reducing the risetime of the control flare had a relatively small effect in weakening the responses. This is because that the flare risetime was short (40 min) compared to the decay time (3 h 20 min), thus more flare energy was contained in the decay phase. The Neupert Effect lead to a larger EUV enhancement during the rising phase of the fast-rise flare, caused a larger maximum ion production enhancement, but the maximum enhancements of the neutral temperature, neutral density, and electron density, were slightly weaker than the control flare owing to the reduction of the risetime, and thus the total energy.

[27] Model simulations showed that the latitude dependence of the thermosphere response was largely determined by the solar zenith angle effect but that the latitude dependence of the ionosphere response was more complicated owing to the effects of the plasma transport and the winter anomaly. Consequently, the latitude variation of the N_mF_2 enhancement showed little dependence on the solar zenith angle effect. The latitude dependence of the TEC enhancement, however, largely followed the solar zenith angle effect due to the dominant contributions from the photochemical production and loss processes, but showing the effects by the $E \times B$ transport and winter anomaly.

[28] Comparisons were made between an X5.4 fast rise (15 min) and short decay (2 h 30 min) flare that occurred on

8 September 2005, and an X6.2 slower rise (40 min) and longer decay (5 h) flare that occurred on 9 September 2005. Both flares were located near the limb of the solar disk. The TIME-GCM simulations show that the neutral density enhancement during the X6.2 flare was 15~20%, whereas the response during the X5.4 flare was only ~5%. The CHAMP neutral density shows a stronger response during the X6.2 flare than during the X5.4 flare, consistent with the simulation results. The simulated and measured TEC enhancements show that the TEC enhancement during the X6.2 flare was ~2–3 times (~5 TECU) of the TEC enhancement during the X5.4 flare (~2 TECU). These simulated and observed results demonstrate that for the flares that have similar magnitudes and the same location on the Sun, the thermosphere and ionosphere responses showed large variability, and the duration (risetime and decay time) of a flare is an important factor in determining the responses.

[29] Diagnostic analysis of the model simulations indicate that the flare response of $E \times B$ caused a strong equatorial anomaly morphology in the electron density enhancement in the F_2 layer, but the equatorial anomaly feature in TEC enhancement was weak owing to the dominant contribution from photochemical production and loss processes. This analysis demonstrates that care must be taken when estimating TEC enhancement using global GPS data. For example, in order to remove the local time effect from the TEC enhancement, the TEC difference between the universal time at the flare peak and the preflare of the previous day is usually subtracted from the TEC difference between the universal time at the flare peak and the preflare on the flare day. However, when geomagnetic forcing between the two days is not negligible, geomagnetic activity effects can cause an equatorial anomaly feature in the TEC enhancement.

[30] In this paper, we examined how a specific flare characteristic affected the thermosphere and ionosphere responses when all the other characteristics were fixed, thus the total energy of the flares was not fixed. The next step is to fix the total energy of a flare, but to change the magnitude, risetime, and decay time, and examine how the thermosphere and ionosphere respond to the variations.

[31] Philippa Browning thanks the reviewers for their assistance in evaluating this paper.

[32] **Acknowledgments.** This research was supported by NASA grants NNX08AQ31G and NNX09AJ60G to the National Center for Atmospheric Research. NCAR is supported by the National Science Foundation.

References

Afraimovich, E. L., A. T. Altynsev, V. V. Grechnev, and L. A. Leonovich (2002), The response of the ionosphere to faint and bright solar flares as deduced from global GPS network data, *Ann. Geophys.*, *45*(1), 31–40.

Bruinsma, S. L., and J. M. Forbes (2007), Global observation of traveling atmospheric disturbances (TADs) in the thermosphere, *Geophys. Res. Lett.*, *34*, L14103, doi:10.1029/2007GL030243.

Chamberlin, P. C., T. N. Woods, and F. G. Eparvier (2007), Flare Irradiance Spectral Model (FISM): Daily component algorithms and results, *Space Weather*, *5*, S07005, doi:10.1029/2007SW000316.

Chamberlin, P. C., T. N. Woods, and F. G. Eparvier (2008), Flare Irradiance Spectral Model (FISM): Flare component algorithms and results, *Space Weather*, *6*, S05001, doi:10.1029/2007SW000372.

Coster, A., and A. Komjathy (2008), Space weather and the Global Positioning System, *Space Weather*, *6*, S06D04, doi:10.1029/2008SW000400.

Davies, K. (1990), *Ionospheric Radio*, Peter Peregrinus, London.

Garcia, H. A. (2000), Thermal-spatial analysis of medium and large solar flares: 1976 to 1996, *Astrophys. J.*, *127*, suppl., 189–210, doi:10.1086/313312.

Hagan, M. E., and J. M. Forbes (2002), Migrating and nonmigrating diurnal tides in the middle and upper atmosphere excited by tropospheric latent heat release, *J. Geophys. Res.*, *107*(D24), 4754, doi:10.1029/2001JD001236.

Hagan, M. E., and J. M. Forbes (2003), Migrating and nonmigrating semidiurnal tides in the upper atmosphere excited by tropospheric latent heat release, *J. Geophys. Res.*, *108*(A2), 1062, doi:10.1029/2002JA009466.

Hedin, A. E., H. G. Mayr, C. A. Reber, N. W. Spencer, and G. R. Carignan (1974), Empirical model of global thermospheric temperature and composition based on data from the Ogo 6 quadrupole mass spectrometer, *J. Geophys. Res.*, *79*, 215–225, doi:10.1029/JA079i001p00215.

Heelis, R. A., J. K. Lowell, and R. W. Spiro (1982), A model of the high-latitude ionospheric convection pattern, *J. Geophys. Res.*, *87*, 6339–6345, doi:10.1029/JA087iA08p06339.

Horan, D. M., R. W. Kreplin, and K. P. Dere (1983), Direct measurements of the gradual extreme ultraviolet emission from large solar flares, *Sol. Phys.*, *85*, 303–312, doi:10.1007/BF00148656.

Jacchia, L. G. (1974), Variations in thermospheric composition: A model based on mass spectrometer and satellite drag data, *J. Geophys. Res.*, *79*, 1923–1927, doi:10.1029/JA079i013p01923.

Keating, G. M., and E. J. Prior (1968), The winter He bulge, *Space Res.*, *8*, 982–992.

Liu, J. Y., C. H. Lin, Y. I. Chen, Y. C. Lin, T. W. Fang, C. H. Chen, Y. C. Chen, and J. J. Hwang (2006), Solar flare signatures of the ionospheric GPS total electron content, *J. Geophys. Res.*, *111*, A05308, doi:10.1029/2005JA011306.

Lühr, H., M. Rother, W. Köhler, P. Ritter, and L. Grunwaldt (2004), Thermospheric up-welling in the cusp region: Evidence from CHAMP observations, *Geophys. Res. Lett.*, *31*, L06805, doi:10.1029/2003GL019314.

McClintock, W. E., G. J. Rottman, and T. N. Woods (2000), Solar STellar Irradiance Comparison Experiment II (SOLSTICE II) for the NASA Earth Observing System's Solar Radiation and Climate Experiment (SORCE) Mission, in *Earth Observing Systems V*, *Proc. SPIE*, *4135*, 225–234.

Mitra, A. P. (1974), *Ionospheric Effects of Solar Flares*, D. Reidel, Boston, Mass.

Neupert, W. N. (1968), Comparison of solar X-ray line emission with microwave emission during flares, *Astrophys. J.*, *153*, L59–L64, doi:10.1086/180220.

Neupert, W. N. (1989), Transient coronal extreme ultraviolet emission before and during the impulsive phase of a solar flare, *Astrophys. J.*, *344*, 504–512, doi:10.1086/167819.

Picone, J. M., A. E. Hedin, D. P. Drob, and A. C. Aikin (2002), NRLMSISE-00 empirical model of the atmosphere: Statistical comparisons and scientific issues, *J. Geophys. Res.*, *107*(A12), 1468, doi:10.1029/2002JA009430.

Priest, E. R. (1981), *Solar Flare Magnetohydrodynamics*, edited by E. R. Priest, Gordon and Breach, New York.

Qian, L., S. C. Solomon, and T. J. Kane (2009), Seasonal variation of thermospheric density and composition, *J. Geophys. Res.*, *114*, A01312, doi:10.1029/2008JA013643.

Qian, L., A. G. Burns, P. C. Chamberlin, and S. C. Solomon (2010), Flare location on the solar disk: Modeling the thermosphere and ionosphere response, *J. Geophys. Res.*, *115*, A09311, doi:10.1029/2009JA015225.

Reigber, C., H. Lühr, and P. Schwintzer (2002), CHAMP mission status, *Adv. Space Res.*, *30*, 129–134.

Richmond, A. D., E. C. Ridley, and R. G. Roble (1992), A thermosphere/ionosphere general circulation model with coupled electrodynamics, *Geophys. Res. Lett.*, *19*, 601–604.

Rideout, W., and A. Coster (2006), Automated GPS processing for global total electron content data, *GPS Solut.*, *10*, 219–228, doi:10.1007/s10291-006-0029-5.

Roble, R. G., and E. C. Ridley (1987), An auroral model for the NCAR thermosphere general circulation model (TGCM), *Ann. Geophys., Ser. A*, *5*(6), 369–382.

Roble, R. G., E. C. Ridley, A. D. Richmond, and R. E. Dickinson (1988), A coupled thermosphere/ionosphere general circulation model, *Geophys. Res. Lett.*, *15*, 1325–1328.

Roble, R. G., and E. C. Ridley (1994), A thermosphere-ionosphere-mesosphere-electrodynamics general circulation model (TIME-GCM): Equinox solar cycle minimum simulations (30–500 km), *Geophys. Res. Lett.*, *21*, 417–420, doi:10.1029/93GL03391.

Solomon, S. C., and L. Qian (2005), Solar extreme-ultraviolet irradiance for general circulation models, *J. Geophys. Res.*, *110*, A10306, doi:10.1029/2005JA011160.

Sutton, E. K., J. M. Forbes, R. S. Nerem, and T. N. Woods (2006), Neutral density response to the solar flares of October and November, 2003, *Geophys. Res. Lett.*, *33*, L22101, doi:10.1029/2006GL027737.

Tsurutani, B. T., et al. (2005), The October 28, 2003 extreme EUV solar flare and resultant extreme ionospheric effects: Comparison to other Halloween events and the Bastille Day event, *Geophys. Res. Lett.*, *32*, L03S09, doi:10.1029/2004GL021475.

Woods, T. N., F. G. Eparvier, S. M. Baily, P. C. Chamberlin, J. Lean, G. J. Rottman, S. C. Solomon, W. K. Tobiska, and D. L. Woodraska (2005), Solar EUV Experiment (SEE): Mission overview and first results, *J. Geophys. Res.*, *110*, A01312, doi:10.1029/2004JA010765.

Woods, T. N., et al. (2008), XUV photometer system (XPS): Improved solar irradiance algorithm using CHIANTI spectral models, *Sol. Phys.*, *250*, 235–267, doi:10.1007/s11207-008-9196-6.

Zhang, D. H., X. H. Mo, L. Cai, W. Zhang, M. Feng, Y. Q. Hao, and Z. Xiao (2011), Impact factor for the ionospheric total electron content response to solar flare irradiation, *J. Geophys. Res.*, *116*, A04311, doi:10.1029/2010JA016089.

A. G. Burns, L. Qian, and S. C. Solomon, High Altitude Observatory, National Center for Atmospheric Research, Boulder, CO 80307, USA. (lqian@ucar.edu)

P. C. Chamberlin, Solar Physics Laboratory, NASA Goddard Space Flight Center, Greenbelt, MD 20771, USA.